

# Electrochemical Synthesis of Nanostructured Metal-doped Titanates and Investigation of Their Activity as Oxygen Evolution Photoanodes

Lawrence, Matthew; Celorrio, Veronica; Shi, Xiaobo; Yanson, Alex; Adkins, Nicholas; Rodriguez-Lopez, Joaquin; Rodriguez, Paramaconi

DOI:

[10.1021/acsaem.8b00873](https://doi.org/10.1021/acsaem.8b00873)

License:

Other (please specify with Rights Statement)

*Document Version*

Peer reviewed version

*Citation for published version (Harvard):*

Lawrence, M, Celorrio, V, Shi, X, Yanson, A, Adkins, N, Rodriguez-Lopez, J & Rodriguez, P 2018, 'Electrochemical Synthesis of Nanostructured Metal-doped Titanates and Investigation of Their Activity as Oxygen Evolution Photoanodes', *ACS Applied Energy Materials*. <https://doi.org/10.1021/acsaem.8b00873>

[Link to publication on Research at Birmingham portal](#)

## **Publisher Rights Statement:**

This document is the unedited Author's version of a Submitted Work that was subsequently accepted for publication in ACS Applied Energy Materials, copyright © American Chemical Society after peer review. To access the final edited and published work see <https://pubs.acs.org/doi/10.1021/acsaem.8b00873>

## **General rights**

Unless a licence is specified above, all rights (including copyright and moral rights) in this document are retained by the authors and/or the copyright holders. The express permission of the copyright holder must be obtained for any use of this material other than for purposes permitted by law.

- Users may freely distribute the URL that is used to identify this publication.
- Users may download and/or print one copy of the publication from the University of Birmingham research portal for the purpose of private study or non-commercial research.
- User may use extracts from the document in line with the concept of 'fair dealing' under the Copyright, Designs and Patents Act 1988 (?)
- Users may not further distribute the material nor use it for the purposes of commercial gain.

Where a licence is displayed above, please note the terms and conditions of the licence govern your use of this document.

When citing, please reference the published version.

## **Take down policy**

While the University of Birmingham exercises care and attention in making items available there are rare occasions when an item has been uploaded in error or has been deemed to be commercially or otherwise sensitive.

If you believe that this is the case for this document, please contact [UBIRA@lists.bham.ac.uk](mailto:UBIRA@lists.bham.ac.uk) providing details and we will remove access to the work immediately and investigate.

This document is confidential and is proprietary to the American Chemical Society and its authors. Do not copy or disclose without written permission. If you have received this item in error, notify the sender and delete all copies.

## Electrochemical Synthesis of Nanostructured Metal-doped Titanates and Investigation of Their Activity as Oxygen Evolution Photoanodes

Journal:	<i>ACS Applied Energy Materials</i>
Manuscript ID	ae-2018-00873a.R1
Manuscript Type:	Article
Date Submitted by the Author:	n/a
Complete List of Authors:	Lawrence, Matthew; University of Birmingham School of Sport Exercise and Rehabilitation Sciences, Celorrio, Veronica; University College London, Chemistry Shi, Xiaobo; Southern University of Science and Technology, Department of Materials Science and Engineering Wang, Qi; Southern University of Science and Technology, Yanson, Alex; MI DE DOCCS Def. EUV Reticle & Plasma Adkins, Nicholas; University of Birmingham Gu, Meng; Southern University of Science and Technology, Department of Materials Science and Engineering Rodríguez-López, Joaquín; University of Illinois at Urbana-Champaign, Department of Chemistry Rodriguez, Paramaconi; University of Birmingham, School of Chemistry

SCHOLARONE™  
Manuscripts

# Electrochemical Synthesis of Nanostructured Metal-doped Titanates and Investigation of Their Activity as Oxygen Evolution Photoanodes

*Matthew J. Lawrence<sup>†,‡</sup>, Veronica Celorrio<sup>§</sup>, Xiaobo Shi<sup>⊥</sup>, Qi Wang<sup>⊥</sup>, Alex Yanson<sup>||</sup>, Nicholas J. E. Adkins<sup>○</sup>, Meng Gu<sup>⊥,\*</sup>, Joaquín Rodríguez-López<sup>∇\*</sup> and Paramaconi Rodriguez<sup>†,‡,\*</sup>*

<sup>†</sup>School of Chemistry, <sup>‡</sup>Birmingham Centre for Strategic Elements and Critical Materials and

<sup>○</sup>School of Metallurgy Materials, University of Birmingham, Edgbaston, Birmingham B15 2TT, United Kingdom

<sup>§</sup>UK Catalysis Hub, Research Complex at Harwell, RAL, Oxford, OX11 0FA, United Kingdom and Kathleen Lonsdale Building, Department of Chemistry, University College London, Gordon Street, London, WC1H 0AJ, United Kingdom

<sup>⊥</sup>Department of Materials Science and Engineering, Southern University of Science and Technology, No. 1088 Xueyuan Blvd, Shenzhen, Guangdong 518055, China

<sup>||</sup>MI DE DOCCS Def. EUV Reticle & Plasma, ASML, De Run 6501, 5504 DR Veldhoven, Netherlands

<sup>∇</sup>Department of Chemistry, University of Illinois at Urbana–Champaign, Urbana, Illinois 61801, United States

KEYWORDS

Electrochemical synthesis, titanate nanowires, mixed metal oxides, photoelectrochemistry, oxygen evolution reaction

## ABSTRACT

Mixed and doped metal oxides are excellent candidates for commercial energy applications such as batteries, supercapacitors, solar cells and photocatalysis due to their activity, stability, tailorable band edge and bandgaps, and low cost. However, the routes commonly employed in their synthesis present synthetic bottlenecks with reliance on sacrificial materials, the use of high temperatures, long reaction times, and little ability to control morphology, thus compromising their scale-up. Herein, we present the single pot, electrochemical synthesis of high surface area, doped metal titanate nanostructures, including  $\text{Na}_2\text{Ti}_3\text{O}_7$  (NTO), 25 wt.% Sn:NTO, 5 wt.% Fe:NTO and 3 wt.% Cu:NTO. The synergic use of the cathodic corrosion method with suspended droplet alloying (SDA) led to materials with excellent homogeneity, presenting a promising route for the screening, production and discovery of electroactive materials. As proof of concept of the synthetic control and impact on reactivity, we found that the photoanodic oxygen evolution activity of the nanomaterials was adversely affected by Fe and Sn doping into NTO while Cu doping, at 3 wt.% displayed significant improvement. This work demonstrates the ability of the cathodic corrosion method to obtain compositionally- and structurally- controlled mixed-metal oxides in a rapid fashion, thus creating new opportunities in the field of materials engineering and the systematic study of compositional gradients on the (photo)electrochemical performance of metal oxide nanoparticles.

## Introduction

Addressing fundamental kinetic and efficiency challenges of electrochemical renewable energy technologies is crucial towards making them more economically viable, thus

contributing to the transition from fossil fuel dependence.<sup>1</sup> A major drawback associated with solar and wind technologies is the intermittent nature of these resources, making the conversion of electrical to chemical energy and its subsequent storage the preferred route.<sup>2-4</sup> In this regard, nanostructured titanium oxides and titanates are an ever increasingly important class of semiconductor materials for energy storage and conversion, due to their high surface areas, natural abundance, low toxicity, and excellent stability,<sup>5-7</sup> which have led to their investigation for a myriad of applications, such as carbon capture technologies,<sup>8</sup> batteries,<sup>9-10</sup> supercapacitors,<sup>11-13</sup> solar cells<sup>14-16</sup> and photocatalysis.<sup>17-18</sup>

As proof of concept of the impact of compositional control on the electroactivity of metal oxide nanoparticles, we explore the activity of doped titanate particles towards photoelectrochemical (PEC) water oxidation. The prospect of converting solar light and electrical energy has resulted in a wealth of literature dedicated to gaining a fundamental understanding of the materials capable of performing PEC reactions, in addition to the development of new materials synthesis strategies.<sup>19</sup> The PEC oxygen evolution reaction (OER), where the absorption of light by semiconductors with band gap >1.23 eV generates reactive charge carriers in order to drive uphill electrochemical reactions, is the rate-determining process for PEC cells.<sup>20</sup> The relatively large band gap of Ti-based oxides (~3 eV) renders them unable to absorb any significant portion of the solar spectrum. Common avenues explored in attempts to extend the visible light absorption properties of the oxides to harness greater portions of the solar spectrum include surface sensitization, via decoration with plasmonic particles and/or narrow band gap semiconductors, as well as the introduction of dopants.<sup>18, 21-22</sup> Doping with earth-abundant metals, especially Cu, Fe and Sn, has been shown to enhance visible light absorption via band gap narrowing and reduced rates of surface recombination.<sup>23-31</sup> Furthermore, nanostructuring and morphological tuning further enhance physical properties through quantum confinement.<sup>17, 32-33</sup> Nanostructuring has

emerged as a promising pathway for materials preparation because of the improved physiochemical properties relative to conventional nanoparticles.<sup>6</sup> In particular, nano-wires/rods/tubes/ribbons benefit from more efficient light absorption, longer charge carrier diffusion lengths due to increased length-to-diameter ratios and increases in specific surface area and the number of active sites.<sup>5-6</sup>

Current approaches for the production of titanate nanomaterials can be categorized into four groups: (i) solid state, (ii) template-assisted, (iii) hydrothermal and (iv) electrochemical. Solid state syntheses involve the calcination of metal powders for long time periods, typically at least 12 hours, with the ability to introduce dopants with a suitable precursor.<sup>34</sup> However, this methodology does not allow for control over the shape, size or morphology of the products. Template-assisted syntheses employ the use of well-ordered, nanostructured substrates onto which the titanates are grown or deposited, commonly via sol-gel methods, chemical vapor deposition or atomic layer deposition (ALD).<sup>35</sup> The sol-gel route involves the deposition of polymer sols onto the substrate and calcination to yield the (doped) titanate product.<sup>15, 26, 29</sup> ALD generates a uniform film over large areas of the template surface, allows for fine control over the thickness and composition of the as-deposited film and can be used to generate three-dimensional structures.<sup>9, 36</sup> The template-assisted methodology is heavily reliant on the underlying template, which is often a sacrificial component of the synthetic process, as in the case of anodized alumina, for determining the shape, size, and morphology of the titanates. This makes the screening and discovery of new materials costly and inconvenient.

By far, the hydrothermal synthesis of nanostructured titanates is the most common approach reported in the literature, after Kasuga et al. first demonstrated the formation of titanate nanotubes in a one-pot procedure without the need for a sacrificial template.<sup>37</sup> Since then, it has been successfully applied to the formation of transition metal-doped titanates.<sup>31, 38-</sup>

<sup>39</sup> Typically, a Ti precursor is reacted with a high molarity NaOH solution, at elevated temperatures and pressures, in a one-pot synthesis, to yield one-dimensional titanate nanostructures, with near complete conversion of the precursor. The structure of the titanates can be varied by choice of solvent, the reaction time, temperature and pressure.<sup>7</sup> However, long reaction times (>24 hours) are typical of such syntheses due to the slow reaction kinetics and room-temperature syntheses require much longer synthesis times (72 hours).<sup>40</sup> Overall, the aforementioned routes are cumbersome due to multiple reaction steps, energy inefficient due to the high temperatures involved in their synthesis, and chemically inefficient due to the use of organic additives, which require additional purification or sacrificial templates and are not cost effective for scale-up.

In contrast, electrochemical routes have been shown to greatly reduce the time taken to produce nanostructured titanate catalysts.<sup>41-42</sup> Electrodeposition is a one-pot technique that enables: (i) control over deposition thicknesses, (ii) direct deposition of the catalyst onto the conductive substrate, maximizing the electrical connection, (iii) ease of access to multi-component, mixed metal oxide materials.<sup>42-44</sup> Unfortunately, control over the uniform morphology of the electrodeposits is lacking. Electrochemical anodization of Ti foils addresses these morphology issues by the generation of titanate nanotube arrays with uniform pore sizes and lengths that can be varied by adjusting the synthetic parameters, such as temperature, electrolyte and anodization potential and duration.<sup>5, 42, 45</sup> However, the syntheses involve the use of organic solvents and demonstration of the production of homogeneously metal-doped titanates via anodization is yet to be reported.

Here we present a new approach for the facile preparation of metal-doped sodium titanate,  $\text{Na}_2\text{Ti}_3\text{O}_7$ , (M:NTO) nanomaterials through the combination of two versatile synthetic techniques: combinatorial alloy laser fabrication<sup>46-47</sup> and cathodic corrosion (Figure 1A-B).<sup>48-</sup>

<sup>49</sup> The synergy of these techniques resides on the ability of obtaining compositionally and

1 structurally well-defined nanomaterials from a small portion of an alloy sample.  
2  
3 Combinatorial alloy laser fabrication significantly reduces the time taken to generate these  
4  
5 alloys and affords the ability to fine tune their composition by variation of wire feed rates and  
6  
7 diameters. Utilization of a high-power laser and suspended droplet alloying (SDA) allowed  
8  
9 the formation of an alloy from thin wires only at the laser focal point, minimized domain  
10  
11 segregation and removed the need to melt bulk materials, thus improving the cost and energy  
12  
13 efficiency.<sup>47</sup> Subsequent electrochemical synthesis was performed via cathodic corrosion<sup>48</sup> to  
14  
15 generate suspended nanoparticles of the metal alloys, in the absence of surfactants, to yield  
16  
17 clean, useable materials.  
18  
19  
20  
21

22 Cathodic corrosion, is a versatile electrochemical synthetic tool (Figure 1B) that has been  
23  
24 demonstrated in both aqueous and organic media, used for the synthesis of both pure metallic  
25  
26 and alloy nanomaterials, with exercisable control, resulting in homogenous particle size and  
27  
28 alloy composition.<sup>50-52</sup> In this method, when the cathodic potential is applied to the working  
29  
30 electrode (WE) the metal is reduced to metal anions stabilized by cations from the electrolyte,  
31  
32 different from protons. This intermediate is relatively stable in the absence of an oxidant, but  
33  
34 in the presence of water, oxygen or reactive oxygen species generated *in-situ* at the counter  
35  
36 electrode (CE), the metal anion intermediate is oxidized, forming metal nanoparticles.<sup>53-55</sup>  
37  
38 These nanoparticles can be further oxidized, depending on the electrolyte or metal, resulting  
39  
40 into metal oxide nanoparticles as described here. Recently, we demonstrated the synthesis of  
41  
42 photoactive metal oxides, including  $\text{BiVO}_4$  and  $\text{H}_2\text{WO}_4$  and presented the variation of  
43  
44 particle size with the frequency of the applied AC voltage.<sup>41</sup> We now expand to the synergy  
45  
46 of this technique with SDA for obtaining compositionally and structurally well-defined  
47  
48 nanomaterials. Here, we show that cathodic corrosion of homogenous Ti-based metal alloys  
49  
50 results in homogenous, high surface area, doped titanate photocatalysts and investigate their  
51  
52 activity towards the PEC OER.  
53  
54  
55  
56  
57  
58  
59  
60



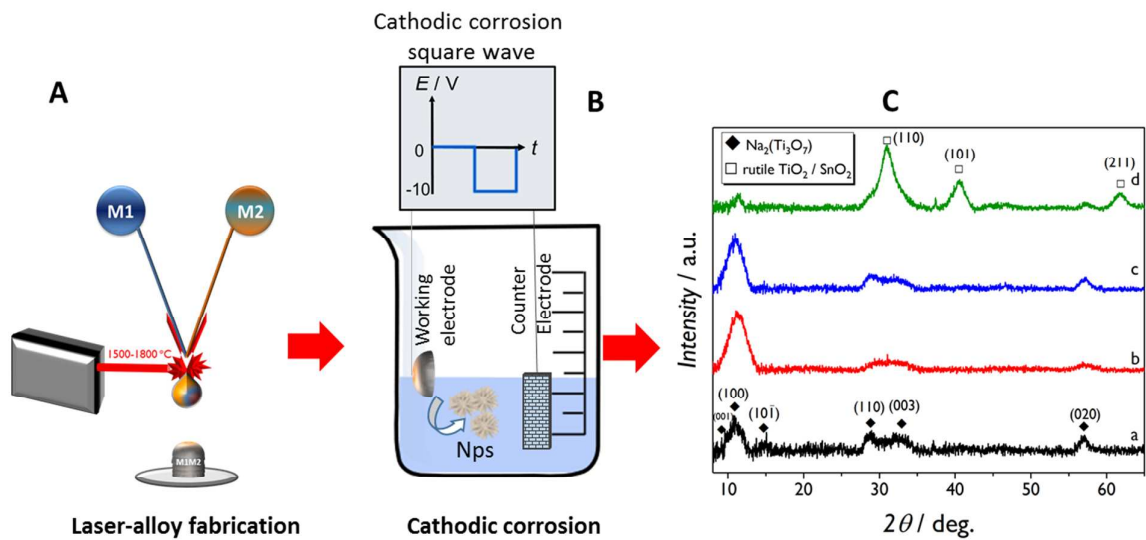


**Figure 1.** (A-B) Schematic representation of alloy and nanoparticle fabrication via the combination of laser combinatorial facility and cathodic corrosion (C) X-ray diffraction patterns of (a) NTO, (b) 5 wt.% Fe:NTO, (c) 3 wt.% Cu:NTO, (d) 25 wt.% Sn:NTO nanoparticles obtained via cathodic corrosion of a Ti wire and Fe<sub>8.82</sub>Ti<sub>91.28</sub>, Cu<sub>6.38</sub>Ti<sub>93.72</sub> and Sn<sub>42.82</sub>Ti<sub>57.18</sub>. The position and assignment of Miller indices were obtained via PDF card no. 01-072-0148 (Na<sub>2</sub>Ti<sub>3</sub>O<sub>7</sub>), JCPDS card no. 21-1276 (rutile TiO<sub>2</sub>) and JCPDS card no. 41-1445 (rutile-type SnO<sub>2</sub>).

## Experimental

### *Alloy laser fabrication*

Homogeneous bulk alloys were prepared via a laser combinatorial facility, as described in a previous report,<sup>47</sup> modified for the production of binary rather than ternary alloys. Pure elemental wires (Advent Research Materials, UK) were aligned into the focal point of a high energy laser beam within a deoxygenated chamber (Ar; flow rate=5 L min<sup>-1</sup>, oxygen level below 50ppm), where alloys were formed through the melting of the wire tips and mixing of the elements, as suspended droplets. Continuous feeding of each wire into the focal point increased the size of the alloy droplet until the mass was great enough so that the gravitational force acting upon it overcame the surface tension of the droplet, causing detachment of the alloy droplet from the wires, causing it to fall onto a stainless-steel substrate (430 grade) positioned below the focal point. Wires were continuously fed into the focal point until the desired amount of alloy was produced, at which point the wire feeding mechanism was shut off and the alloy was allowed to cool in the argon-filled chamber. The typical synthesis time was 2 min. After cooling, alloys were retrieved, removed from the stainless-steel substrates, cut into narrow discs/rods with width ~2 mm by electrical discharge machining (EDM) and then mechanically polished.

### *Cathodic corrosion synthesis*

For the preparation of the nanoparticles the cathodic corrosion method was implemented.<sup>48</sup> Nanoparticles of NTO and M:NTO (M =Fe, Cu or Sn) were synthesized by applying an AC voltage of 0 to -10 V between the WE (Ti wire of 0.25 mm diameter or laser-fabricated Ti-alloy) and a flame-annealed, high surface area Pt flag used as counter electrode, in 10 mL of 10 M NaOH (Merck, ≥99%) solution. Flame annealing is a common terminology used to describe a cleaning process of certain metal electrodes such as Pt, Au or Pd. A propane/butane torch is used to increase the temperature of the electrode and at these

temperatures all organic contaminants are removed from the electrode thus avoiding contaminating the electrochemical measurements. Typically, syntheses were conducted for 1 hour to collect sufficient quantities for all the characterization and the electrocatalytic assessments. The 100 Hz square wave signal was generated by LabVIEW / National Instruments hardware and amplified by a power amplifier. A suspension of oxide particles was formed at the WE in each synthesis. After the synthesis, the nanoparticles were separated by centrifugation and decanting the supernatant. The process was repeated until the removed supernatant was of neutral pH; the oxides were left suspended in milli-Q water (PURELAB Ultra, 18.2 MΩ.cm).

### *Physical Characterization*

The crystal structure of the metal oxides was investigated by X-ray diffraction (XRD) via a Bruker D2 Phaser Powder X-ray diffractometer (Co K $\alpha$  radiation source,  $\lambda=1.78897$  Å; 30 kV operating voltage; 10 mA). Aqueous oxide suspensions were drop-cast onto a quartz crystal in 25  $\mu$ L increments and the water was evaporated in a fan oven (60 °C). Diffraction patterns were recorded for >12 hours.

Particle morphology was analyzed by scanning electron microscopy (SEM) using a Philips XL-30 ESEM instrument. Compositional analyses were conducted via energy dispersive X-ray spectroscopy (EDX/EDS) coupled to the SEM microscope and X-ray fluorescence spectroscopy (XRF) (Bruker S8 Tiger 4 kW spectrometer; He atmosphere). Transmission electron microscopy (TEM) was performed on FEI Themis G2 microscopes, with double Cs-correctors, operating at 300 kV, in scanning transmission electron microscopy (STEM) mode with both bright field and high-angle annular dark field (HAADF) images recorded. The microscopes were also equipped with super-X EDS detectors, which facilitate the acquisition of EDS maps with 50 times higher signal collection efficiency than normal EDS detectors.

The specific surface area was estimated from the transmission electron microscopy images. (see *Supporting Information*).

X-ray absorption spectroscopy (XAS) measurements were recorded on the B18 beamline at Diamond Light Source operating with a ring energy of 3 GeV and at a current of 300 mA.<sup>56</sup> The monochromator comprises Si(111) crystals operating in Quick EXAFS mode. Calibration of the monochromator was carried out using the respective foils prior to the measurements. Pellets of the different samples were collected in fluorescence mode at the Ti K-edge (4965 eV), Fe K-edge (7111 eV), Cu K-edge (8979 eV) and Sn K-edge (29200 eV), simultaneously with the metallic foils. The data was analyzed using Athena and Arthemis programs which implement the FEFF6 and IFEFFIT codes.<sup>57-58</sup>

Optical property characterization was conducted using a Varian Cary 50 UV-Vis spectrophotometer (see *Supporting Information*).

#### *Photoelectrochemical characterization*

Electrodes were prepared by drop-cast deposition of nanoparticle suspensions onto indium tin oxide (ITO) slides (SPI Instruments, 15–30  $\Omega$ ) in volumes of 10–20  $\mu\text{L}$  to generate a photoelectrode; electrical contact to the ITO slide was achieved by securing indium wire to the edge of the conductive face of the slide with conductive copper tape (3 M Electrical Products). The photoelectrode was assembled into a Teflon electrochemical cell ( $\sim 3\text{mL}$  volume) as the WE in a 3-electrode electrochemical setup. A flame annealed Pt wire (1 mm diameter) and Ag/AgCl (3 M KCl) with a  $\text{NaClO}_4$  salt bridge were employed as the counter and reference electrodes, respectively, with 0.1 M NaOH ( $\text{pH} = 12.7$ ) serving as electrolyte. All measurements were conducted at ambient temperature in a dark room. PEC measurements were conducted under illumination by incident polychromatic white light (UV and visible), generated by a 300 W, 6258 Oriel Xe arc lamp (incident light power  $\sim 180\text{ mW cm}^{-2}$ ). Electrode potential and current measurements were controlled and recorded using

CHI920D potentiostats (CHI Instruments). Measured potentials were converted to the reversible hydrogen electrode (RHE) via the Nernst equation.

## Results and Discussion

Prior to the synthesis of the nanoparticles the composition of the alloys used as starting materials was fully characterized by XRD, XRF and EDX (see SI). The analyses confirm that the atomic composition of the starting alloys were:  $\text{Fe}_{8.81}\text{Ti}_{91.18}$ ,  $\text{Cu}_{6.28}\text{Ti}_{93.72}$  and  $\text{Sn}_{42.82}\text{Ti}_{57.18}$ .

After applying the cathodic AC voltage to the starting alloys, white suspensions of nanoparticles were collected from the FeTi and the CuTi samples, whilst a light-grey suspension was observed for SnTi.

### XRD

Figure 1C shows the XRD patterns of the nanowires (NWs) prepared by cathodic corrosion. As curve (a) shows, the diffraction pattern of the titanate nanoparticles present broad peaks at  $2\theta=10.96^\circ$ ,  $14.75^\circ$ ,  $28.68^\circ$ ,  $32.37^\circ$  and  $56.98^\circ$  which correspond to the (100), (10 $\bar{1}$ ), (110), (003) and (020) planes of sodium titanate,  $\text{Na}_2\text{Ti}_3\text{O}_7$  (NTO), in agreement with reports on the generation of NTO nanotubes via other synthetic routes.<sup>38-39, 59-60</sup> The NTO crystal structure (PDF no. 01-072-0148) consists of zig-zagging layers of edge-shared  $\text{TiO}_6$  octahedra, with ionically bonded, intercalated  $\text{Na}^+$  ions (Figure 2B).<sup>61</sup> The observed peak broadening is associated to the low crystallinity and nanostructuring of the NWs. In the case of the Fe:NTO (Figure 1C.b) and Cu:NTO (Figure 1C.c), a decrease in intensity for the (10 $\bar{1}$ ), (110), (003) and (020) signals is observed relative to the (100) signal at  $\sim 11^\circ$  whilst no additional signals are observed, suggestive of successful doping due to a disruption in recurring crystallinity. The decrease in crystallinity can be associated to the Cu and Fe incorporation.  $\text{Cu}^{2+}$  dopant species intercalate between the layers of  $\text{TiO}_6$  octahedra in titanate nanotubes and the number of  $\text{Cu}^{2+}$  intercalated per unit cell is half that of  $\text{Na}^+$ , primarily due to adherence to charge neutrality laws (Figure 2B).<sup>38, 60</sup>

Assuming that the same intercalation process occurs in the case of Fe, the substitution of  $\text{Na}^+$  for  $\text{Fe}^{n+}$ , where  $n \geq 2$ , would cause a contraction of the unit cell. Indeed, shifts in (100) peak position were observed for Fe:NTO and Cu:NTO from  $2\theta=10.96^\circ$  to  $11.25^\circ$  and  $11.00^\circ$ , respectively, indicative of a decrease in lattice parameter, in agreement with literature.<sup>31</sup> This effect is not as pronounced in the case of Cu:NTO due to the low Cu concentration ( $\sim 1$  at.%). Furthermore, previous reports have shown that the incorporation of Fe and Cu as a dopant in the crystalline structure of  $\text{TiO}_2$  does not result in additional XRD signals, in agreement with our results.<sup>29, 62</sup>

Contrastingly, the XRD pattern of the nanoparticles prepared from  $\text{Sn}_{42.82}\text{Ti}_{57.18}$  shows additional intense peaks at  $2\theta=30.94^\circ$ ,  $40.64^\circ$  and  $61.84^\circ$  which could be associated to the (110), (101) and (211) planes of rutile  $\text{TiO}_2$  (Figure 1C.d). The positions of these signals, however, are slightly shifted to lower  $2\theta$  values, suggesting an increase in lattice parameter as a result of Sn-doping. On the other hand, the rutile phase of  $\text{SnO}_2$  also presents signals at similar  $2\theta$  angles (Figure S3), therefore the presence of  $\text{SnO}_2$  was not discarded.<sup>63</sup> Comparison of the diffraction pattern to previously reported Sn-doped titanate materials synthesized by alternative methods suggest that Sn-rich areas exist in and facilitate formation of a predominant rutile phase (Figure S4).<sup>64</sup>

### Morphological and elemental analyses

In order to determine morphology and chemical composition of the samples, SEM-EDX and HAADF STEM-EDS were conducted. Both STEM (Figure 2) and SEM (Figure S5) demonstrated the presence of aggregated NWs for all the samples, in agreement with previous reports on  $\text{TiO}_x$  nanoparticle production via cathodic corrosion,<sup>41, 65</sup> providing evidence for the ability of cathodic corrosion to produce nanostructured titanate materials in the absence of capping agents or surfactants, at ambient temperatures. While surfactants may favor the dispersion of the materials,<sup>66</sup> the presence of surface ligands might strongly affect

the catalytic activity, further complicating particle purification.<sup>67-69</sup> The TEM images show that no significant morphological variation between the undoped (Figure 2A) and doped (Figure 2C-E) materials was observed.

Analysis of the electron micrographs indicated that the diameters of the individual NW samples were  $12.35 \pm 1.92$  nm,  $7.49 \pm 1.04$  nm,  $11.74 \pm 1.92$  nm and  $10.62 \pm 1.55$  nm for NTO, Fe:NTO, Cu:NTO and Sn:NTO, respectively (Figure S6). Due to the aggregated nature of the nanoparticles, the size distribution for the lengths of the NWs was difficult to determine with precision. The lengths were on the order of few hundreds of nanometers. The estimated surface areas were 90.1, 154.7, 96.8 and 107.1 m<sup>2</sup> g<sup>-1</sup>, respectively, for NTO, Fe:NTO, Cu:NTO and Sn:NTO, in reasonable agreement with BET values reported in the literature for analogous nanostructures (see Supporting Information).<sup>17</sup>

We used STEM-EDS analyses (Figure S7) to identify the composition of constituent elements, in addition to the relative metal atomic composition to evaluate the transfer of initial alloy composition to the oxide NWs (Tables S2 & S3). The nanoparticles retained the relative metal composition of the parent alloys, particularly well in the case of 5 wt.% Fe:NTO and 3 wt.% Cu:NTO. While STEM-EDS spectra alone do not provide unambiguous proof of the homogeneity of the samples, with preferential etching and phase segregation as potential masked effects, these experiments represented a first confirmation of the successful implementation of cathodic corrosion on SDA alloys.

For a stricter evaluation of the compositional effectiveness of the syntheses we turned to HAADF-EDS elemental mapping and to HRTEM. These analyses provided further evidence of the excellent homogeneity of constituent elements present in the doped titanate NWs synthesized by cathodic corrosion of laser-fabricated alloys (Figure 2I-Q). No areas of metal segregation or clustering were found within the materials, with both Ti and the dopant metal observed in all regions of the synthesized NWs.

Further HAADF-HRTEM images of 5 wt.% Fe:NTO NWs showed an interlayer distance of 0.75 nm (Figure 2F), in agreement with literature.<sup>70</sup> This is a slight decrease in the NTO (100) interlayer distance relative to the database value, indicative of compression upon Fe intercalation, in agreement with XRD results. Some isolated fringe regions with amorphous structures and the presence of small, spherical crystalline nanoparticles with d-spacing of 0.21 nm, which can be attributed to the (420) plane of  $\text{Fe}_2\text{O}_3$ , were observed (Figure S9). Bright field STEM and HRTEM images of 3 wt.% Cu:NTO show that the sample solely consisted of crystalline NWs, with no other morphology observed (Figure 2D,G). An interlayer distance of 0.747 nm was observed, corresponding to the compressed (100) plane of NTO, similar to that of 5 wt.% Fe:NTO NWs. On the other hand, the 25 wt.% Sn:NTO NWs show an interlayer distance of 0.77 nm for the (100) plane (Figure 2H). This increase in d-spacing relative to the Fe- and Cu-doped NWs is rationalized by the increased size of Sn ions relative to Fe and Cu (Figure 2B) and to the higher concentration of the Sn-dopant in this sample. Additionally, cubic planes with interlayer distances of 0.26 nm and 0.35 nm were observed via atomic STEM, corresponding to the (101) and (110) planes of rutile  $\text{SnO}_2$ , respectively – JCPDS no. 41-1445 – providing further evidence of the existence of both Sn-doped titanate NWs and  $\text{SnO}_2$  in the 25 wt.% Sn:NTO sample, in agreement with XRD results (Figure S10). Altogether, the observed crystallinity and interlayer distances of the doped NWs are in good agreement with analogous transition metal-doped nanostructured titanates synthesized by alternative routes,<sup>71-74</sup> showcasing the advantage of the use of cathodic corrosion to rapidly produce M:NTO nanostructures by the single-step, electrochemical etching of alloys at ambient temperature.



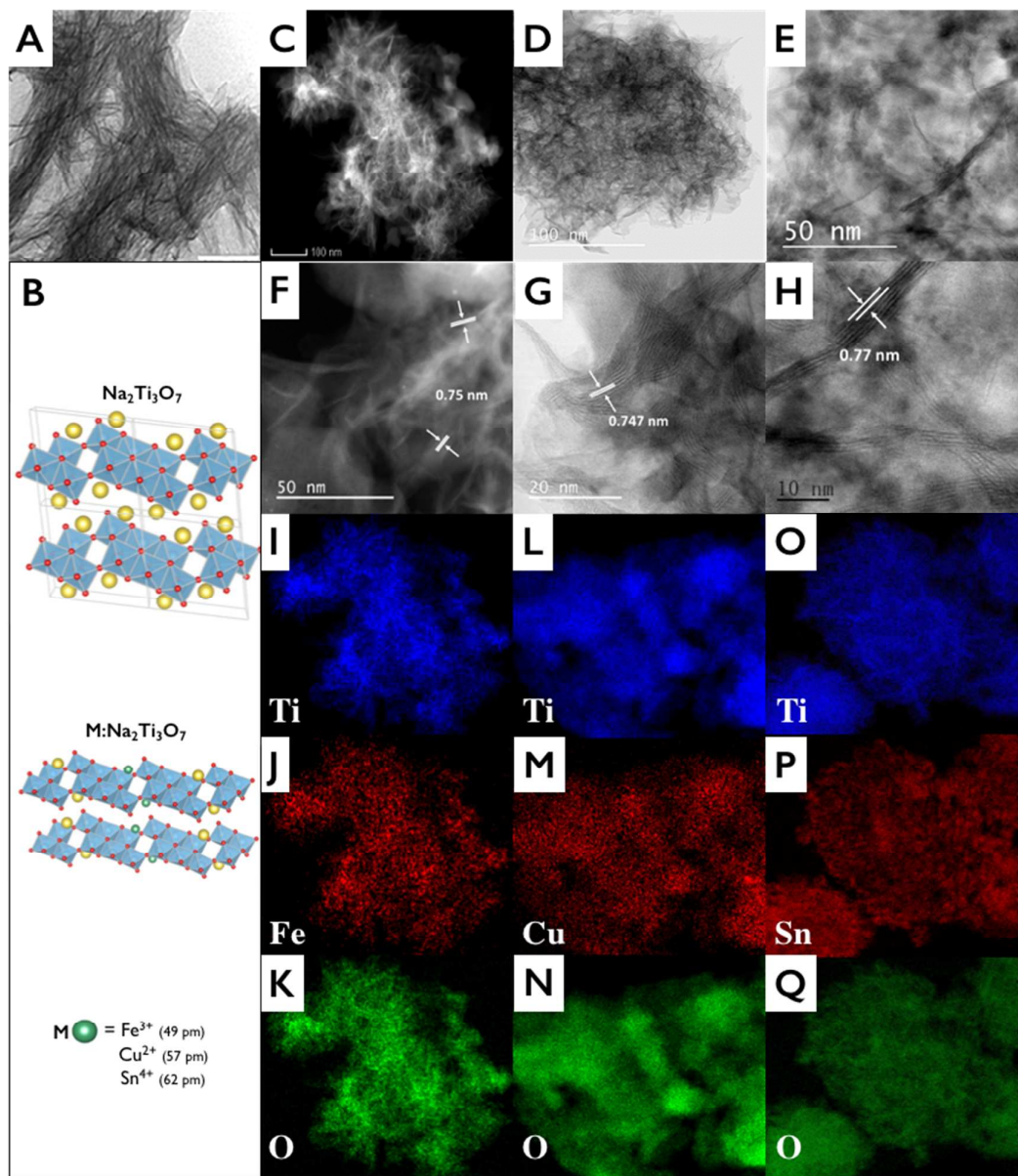


**Figure 2.** (A) Low magnification TEM image of NTO NWs. (B) Crystal structures of NTO and intercalated transition metal-doped analogues, M:NTO. (C) HAADF-STEM image of 5 wt.% Fe:NTO, (D-E) bright field STEM images of 3 wt.% Cu:NTO and 25 wt.% Sn:NTO NWs, respectively. (F) Dark field and (G-H) bright field HRTEM images of 5 wt.% Fe:NTO, 3 wt.% Cu:NTO and 25 wt.% Sn:NTO NWs, respectively. HAADF-EDS elemental mapping for (I-K) 5 wt.% Fe:NTO, (L-N) 3 wt.% Cu:NTO and (O-Q) 25 wt.% Sn:NTO.

XAS

More detailed information about the bonding environment and the oxidation states of the metal constituents of the NWs formed via cathodic corrosion were determined by XAS. Figure 3A compares the normalized Ti K-edge XANES spectra of the synthesized M:NTO samples against Ti foil,  $\text{Ti}_2\text{O}_3$ , and  $\text{TiO}_2$  standard compounds. Pre-edge features are sensitive to valence, occurring  $\sim 2.0$  eV lower in  $\text{Ti}^{3+}$  samples compared to  $\text{Ti}^{4+}$ .<sup>75</sup> All the spectra show only a weak pre-edge peak relative to Ti foil due to the octahedral local structures around Ti ions.<sup>76</sup> Additionally, the pre-edge features observed for the M:NTO samples display the best agreement with features reported for titanate structures rather than for either anatase or rutile  $\text{TiO}_2$ .<sup>75</sup> It is challenging to deduce unambiguously the Ti valence because the pre-edge features vary as a function of Ti coordination. However, the edge positions, defined as the maximum of the first-derivative, suggest that Ti atoms in the M:NTO nanoparticles exist in a +4 oxidation state (Figure S11A). Furthermore, the emergence of the pre-edge feature at 4974 eV for 25 wt.% Sn:NTO corresponds to rutile  $\text{TiO}_2$ ,<sup>75</sup> further suggesting the presence of the rutile phase in the sample, consistent with our XRD and SEM-EDX analyses.

Figure 3B shows the Fe K-edge XANES spectra of the reference foil and oxide compounds in comparison to the 5 wt.% Fe:NTO NWs. The first-derivative peak of the absorption coefficient appears at 7120.5 eV for  $\text{Fe}^{2+}$ , while that for  $\text{Fe}^{3+}$  appears at 7124 eV.<sup>77</sup> Interestingly, for 5 wt.% Fe:NTO, this first-derivative peak appears at around 7124.2 eV (Figure S11B), corresponding to a Fe oxidation state  $\geq +3$ , which has been ascribed previously to an electronic inductive effect promoted by surrounding  $\text{Ti}^{4+}$  ions.<sup>78</sup>

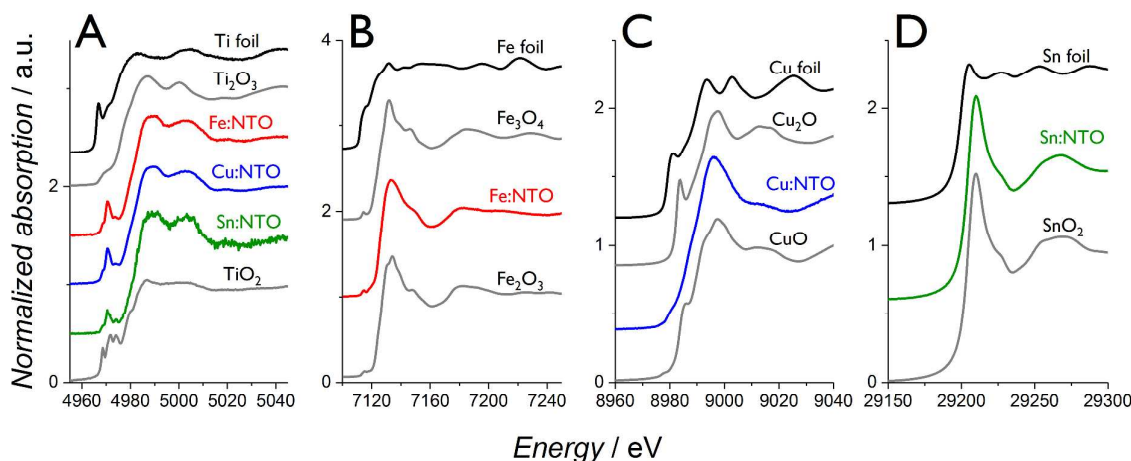


**Figure 3.** Normalized (A) Ti K-edge, (B) Fe K-edge, (C) Cu K-edge and (D) Sn K-edge XANES spectra of 5 wt.% Fe:NTO, 3 wt.% Cu:NTO and 25 wt.% Sn:NTO nanoparticles synthesized via cathodic corrosion of laser-fabricated alloys compared to the reference compounds; metallic foils and standard metal oxide compounds are represented by black lines and grey lines, respectively.

Figure 3C illustrates the characteristic XANES spectra of Cu foil,  $\text{Cu}_2\text{O}$  and  $\text{CuO}$  standard compounds together with Cu K-edge of the synthesized 3 wt.% Cu:NTO NWs. The edge position was found to be 8979.0, 8980.6 and 8983.6 eV for Cu foil,  $\text{Cu}_2\text{O}$ , and  $\text{CuO}$ , respectively, in agreement with values reported in the literature.<sup>79-81</sup> The first-derivative peak for Cu:NTO indicated that  $\text{Cu}^{2+}$  is present (Figure S11C). However, the near edge structure did not allow for the unambiguous determination of the corresponding Cu coordination.

Finally, Figure 3D shows the Sn K-edge XANES spectra for 25 wt.% Sn:NTO as well as the reference spectra of Sn foil and  $\text{SnO}_2$ . The edge of the Sn foil was located at 29200 eV, in agreement with data in the literature.<sup>82</sup> The edge position of 25 wt.% Sn:NTO corresponds to 29204 eV, which is the value measured for the  $\text{SnO}_2$  reference, indicating that the Sn exists as tetravalent  $\text{Sn}^{4+}$  ions (Figure S11D). The appearance of the 25 wt.% Sn:NTO spectra closely resembles that of  $\text{SnO}_2$ , suggesting that  $\text{SnO}_2$  is present.

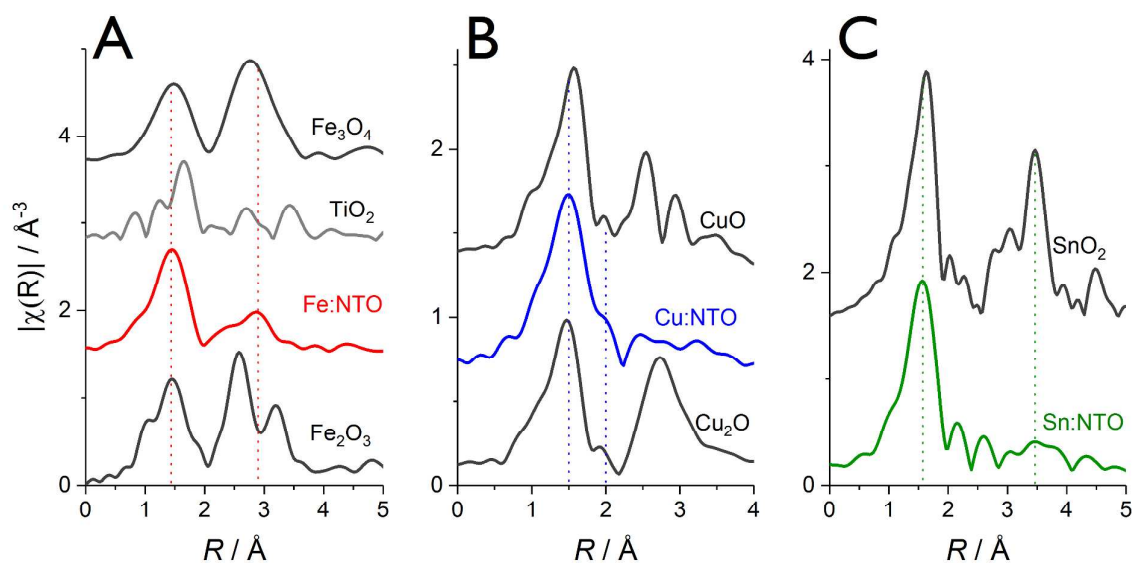


**Figure 4.** EXAFS Fourier Transforms of  $k^2\chi(k)$  functions for (A) Fe K-edge, (B) Cu K-edge and (C) Sn K-edge. The spectra for the standard oxide compound references are shown for comparison.

Figure 4A shows the Fe K-edge EXAFS Fourier transforms (FTs) of 5 wt.% Fe:NTO in addition to the  $\text{Fe}_2\text{O}_3$ ,  $\text{Fe}_3\text{O}_4$  and  $\text{TiO}_2$  standard compound references. The FT spectra show two strong peaks below 4 Å. The first, at around 1.5 Å (without phase correction), corresponds to the first coordination shell (Fe-O) and matches well with the first strong peak identifiable in the FT spectrum of  $\text{Fe}_3\text{O}_4$ . A quick first shell fit resulted in a coordination number of  $\sim 4$  for the Fe-O path, and a bond distance of 1.94 Å. The second peak around 3 Å is associated with the second coordination shell, with potential Fe-Fe, Fe-Ti and Fe-O contributions together with multiple scattering paths. Looking at the data qualitatively, the formation of  $\text{Fe}_2\text{O}_3$  and  $\text{Fe}_3\text{O}_4$  can be ruled out as the FT of the NWs is quite different, particularly above 3 Å. Moreover, the position of the second shell peaks differs from that of Ti-Ti<sub>1</sub> for  $\text{TiO}_2$ , suggesting that the Fe atoms do not simply substitute for Ti. The fit data in  $k$ -space and the corresponding fitted parameters at the Fe K-edge are reported in Figure S12(A,B) and Table S3.

Figure 4B shows Cu K-edge EXAFS FTs of 3 wt.% Cu:NTO and the reference samples. The first peak at  $\sim 1.5$  Å (phase shift was not corrected) is due to the Cu-O scattering in the first shell. The second coordination peaks – between 2 and 3 Å – are weak in comparison to the CuO reference but are not absent, suggesting a scattering from a heavier element. However, both SEM-EDS and TEM-EDS analyses rule out the presence of elements heavier than Cu in the sample. Additionally, it has been reported that a noticeable second shell EXAFS feature at  $\sim 2.4$  Å is observed in CuO and Cu-doped titanate nanotubes, attributable to the presence of Cu-Cu bonding interactions.<sup>83-84</sup> Comparison of our Cu K-edge EXAFS spectra to the literature indicate that Cu-Cu bonding in our sample is of low occurrence, as this feature is not present. Additionally, the poor resolution of the higher shell features, including Cu-Ti bonding ( $>3$  Å), limit the depth of discussion.<sup>83</sup> A quick first shell fit was performed to the data using one oxygen scattering path (Figure S12 C&D and Table S4), resulting in a coordination number  $N=3.5$  at Cu-O distance of 1.93 Å, suggesting that the Cu is in a tetrahedral coordination, in agreement with existing literature.<sup>84</sup>

At the Sn K-edge (Figure 4C), the EXAFS spectrum of 25 wt.% Sn:NTO is dominated by the Sn-O coordination, suggestive of the formation of either a SnO<sub>2</sub> layer or isolated SnO<sub>2</sub> particles, in agreement with XRD, SEM-EDX and STEM-EDS analysis. The Sn-Ti interaction was not detected, which could be attributed to the fact that it is too small compared with the Sn-O signal or non-existent. The EXAFS data and the corresponding fitted parameters at the Sn K-edge reported in Figure S12(E,F) and Table S5, confirmed an octahedral coordination of Sn. Unfortunately, the Ti K-edge EXAFS functions are not usable because of poor statistics.

#### Summary of physical characterization

The combination of the different physicochemical characterization techniques suggests that crystalline NTO NWs are synthesized by electrochemically etching Ti electrodes in 10 M

NaOH under an applied AC voltage of 0 to -10 V. The NWs agglomerate to form discrete particles with high surface area and metal doped titanates with analogous structure are produced when Ti alloys are employed. STEM-EDS and SEM-EDX confirm excellent homogeneity of constituent elements in all cases. XAS and XRD suggest that the dopant metal cations predominantly intercalate between Ti-O octahedral layers rather than substituting for Ti and that the binary oxides of the dopant metal are absent in the case of Fe and Cu. For 25 wt.% Sn:NTO, where the concentration of Sn in the parent alloy was > 40 at.%, XRD, XAS, SEM-EDX, STEM (Figure S8) and HRTEM all indicate the presence of rutile SnO<sub>2</sub> in addition to Sn-doped TiO<sub>2</sub> and titanate NWs, suggesting that non-trivial differences in the rate of chemical oxidation for atomized Ti and Sn exist.

#### Evaluation of PEC activity

Chronoamperometry (*I-t*) under interrupted illumination measurements were employed to determine the PEC properties of the oxide nanomaterials in aqueous 0.1 M NaOH. The selection of potential at which the photocurrents were measured was based on the comparison of CV response in the dark and under illumination (Figure S14). Figure 5 shows that charge-carrier recombination transients were observed during the 'on' portion of the chopped light cycles in all *I-t* curves, additional evidence of PEC activity.<sup>32</sup> At 1.5 V vs RHE the M:NTO samples did not display significant improvement towards OER in comparison with the undoped titanate nanocatalyst, in agreement with *J-E* curves under interrupted illumination (Figure S15). At a more oxidative potential (1.8 V vs RHE), reduced photocurrents were measured on 5 wt.% Fe:NTO and 25 wt.% Sn:NTO. The Fe(III) oxidation state, determined by XANES analysis, is reported to cause an increase in bulk photogenerated charge carrier recombination by serving as hole traps, thereby limiting the flux of holes to the surface to conduct the OER and reducing the relative magnitude of photocurrents measured.<sup>85-86</sup> In the case of the Sn-doped titanate, because the Fermi level of SnO<sub>2</sub> is lower than that of TiO<sub>2</sub>, it

was expected that the photogenerated electrons would transfer from the NTO to the  $\text{SnO}_2$ , resulting in a reduction of the number of photogenerated electrons on the surface of NTO and subsequent surface-recombination events. However, STEM characterization of the 25 wt.% Sn:NTO sample suggest that the  $\text{SnO}_2$  present in the sample acts as a passivating shell atop the Sn:NTO NWs. In this scenario, the photogenerated holes that migrate to the surface of the Sn:NTO are prone to undergo annihilation with the increased electron occupancy of the  $\text{SnO}_2$  shell conduction band, thereby decreasing the observed PEC activity.

Interestingly, 3 wt.% Cu:NTO nanoparticles demonstrated a significant increase in the steady-state photocurrent for the OER in comparison with the undoped titanate. UV-vis absorption spectroscopy indicated that 3 wt.% Cu:NTO possessed enhanced light absorption capabilities relative to NTO, in addition to enhanced absorption intensity in the visible region (Figure S13). Doping  $\text{TiO}_2$  with Cu is reported to decrease the magnitude of its band gap by lowering the position of the conduction band and the introduction of inter-band levels by spin-up Cu 3d states.<sup>38, 87</sup> The combination of these two effects serves to increase the visible light absorption capabilities of  $\text{TiO}_2$ . Thus, we anticipate that an analogous effect is wrought in the case of NTO and is the main contributor to the observed relative increase in photocurrent upon doping with  $\text{Cu}^{2+}$ . The magnitude of the current transients were also larger indicating an increase in charge-carrier recombination, which can be attributed to an increase in electron flux due to the presence of Cu dopants. Increases in catalyst loading and subsequent increases in photocurrent and recombination transients, further demonstrated the PEC catalytic properties of 3 wt.% Cu:NTO towards the OER (Figure S16).

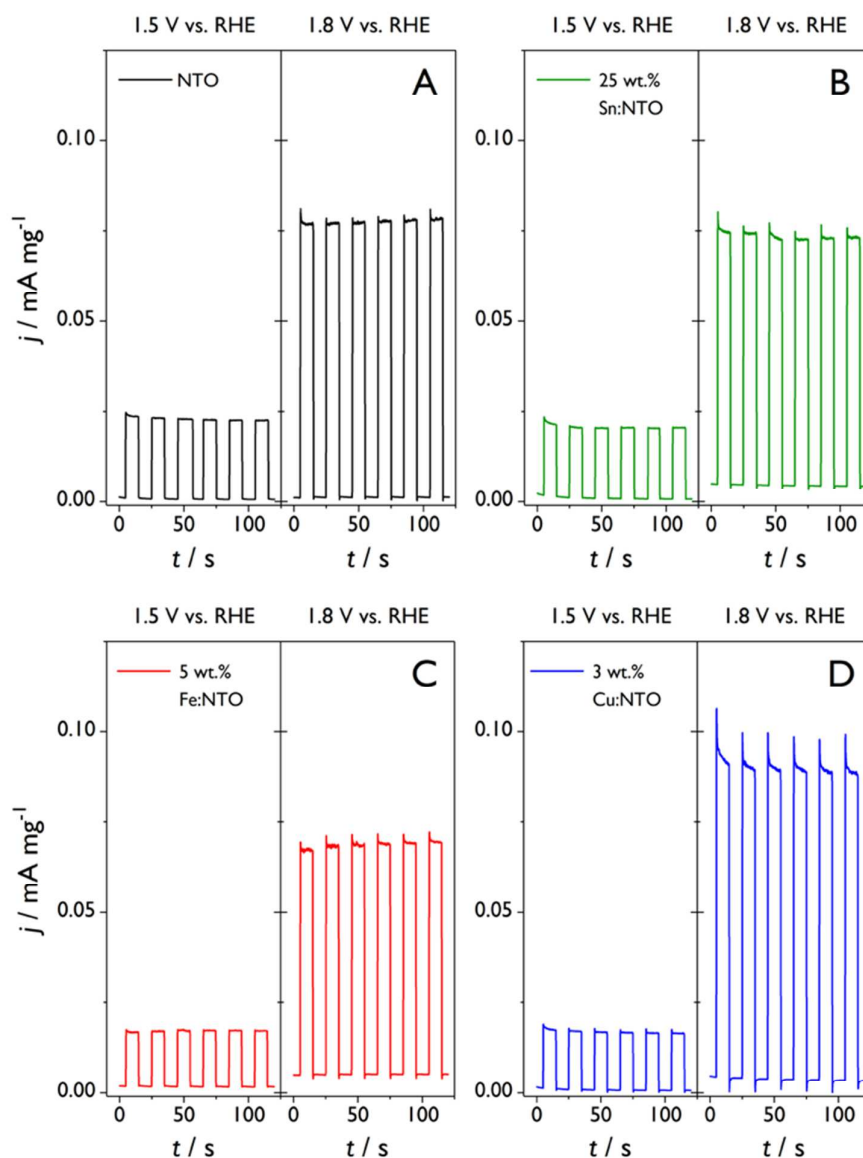


**Figure 5.** Chopped light  $I$ - $t$  curves, at 1.5 V ( $\eta \sim 300$  mV) and 1.8 V ( $\eta \sim 500$  mV) vs. RHE in 0.1 M NaOH, of titanate nanoparticles synthesized via cathodic corrosion: (A) NTO, (B) 25 wt.% Sn:NTO, (C) 5 wt.% Fe:NTO and (D) 3 wt.% Cu:NTO. The potentials displayed correspond to OER overpotentials of  $\sim 300$  mV and 500 mV, respectively.

The improvement in PEC activity for 3 wt.% Cu:NTO prompted investigation of the effect of increasing Cu content. Accordingly, a laser-fabricated  $\text{Cu}_{19.31}\text{Ti}_{80.68}$  alloy was employed as WE. The suspension obtained from the electrochemical synthesis possessed a pale blue tint



(Figure S17) which disappeared during the electrolyte removal centrifugation process. XRD patterns suggested that attempts to increase the Cu dopant concentration were successful. A shift in the NTO (100) peak position from  $11.00^\circ$  to  $11.39^\circ$ , relative to 3 wt.% Cu:NTO, indicated a decrease in lattice parameter whilst observed signal broadening was indicative of a decrease in long-range crystallinity (Figure S18A). STEM-EDS analyses (Figure S18B) revealed that aggregated NWs had been produced but the relative composition of Cu was noticeably lower in the titanate than in the parent alloy, 9 wt.% (4 at.%) (Table S7). Comparison of only the relative metal atomic ratios of Cu and Ti in the NWs and the alloy precursor revealed reasonable agreement between the parent alloy and the NWs (Table S7).

In order to investigate the cause of the blue tint observed in the 9 wt.% Cu:NTO suspension, a Cu wire was subjected to cathodic corrosion under identical conditions to the alloys. A clear, light-blue aqueous solution of  $\text{Cu}(\text{OH})_2/\text{Cu}(\text{OH})_4^{2-}$  (Figure S18C) confirmed that Cu is susceptible to form aqueous metal complexes under the specific cathodic corrosion conditions employed (AC voltage between 0 and -10 V; 100 Hz squarewave; 10 M NaOH electrolyte) and provides a plausible explanation for the low Cu content observed in the nanoparticles. In addition, the presence of peaks at  $2\theta = 51.62^\circ$  and  $60.35^\circ$  in the XRD pattern of the  $\text{Cu}_{19.32}\text{Ti}_{80.68}$  alloy, corresponding to the (111) and (200) planes of fcc Cu, not observed for  $\text{Cu}_{6.28}\text{Ti}_{93.72}$ , suggest the presence of Cu and Ti metal segregation at higher alloying concentrations (Figure S18D). The reduced content of Cu in the 9 wt.% Cu:NTO NWs can be explained by the low limit of incorporation of Cu ions into  $\text{TiO}_2$ .<sup>60, 62</sup> Albeit a significantly larger concentration of copper was not achieved, the HAADF-STEM imaging and EDS elemental mapping demonstrated that the Cu and Ti were homogeneously distributed throughout the 9 wt.% Cu:NTO NWs (Figure 6A). Negligible differences in the Cu K-edge XANES (Figure 6B) and EXAFS (Figure 6C) spectra were observed. However, the second shell interactions observed at the Cu K-edge (Cu-Cu or Cu-Ti) have more resolved distances

1  
2  
3 in the case of 9 wt.% Cu:NTO, where the Cu content is higher and thus the relative frequency  
4 of the interactions is increased. Additionally, FT EXAFS simulated fits for the sample with  
5 increased Cu content have a lower value for the  $R_{\text{factor}}$  (Figure S19 and Table S4). Albeit that  
6 the visible light absorption intensity for 9 wt.% Cu:NTO was enhanced relative to NTO, 3  
7 wt.% Cu:NTO possessed greater absorption at all wavelengths (Figure S20).  
8  
9

10  
11  
12  
13 The PEC results (Figure 7) further demonstrated that Cu:NTO nanomaterials produced via  
14 cathodic corrosion of laser-fabricated alloys are photoelectrochemically active towards OER.  
15 However, increasing the relative Cu dopant concentration did not yield any increase in PEC  
16 activity, in agreement with the UV-vis analysis. Rather, photocurrent density was reduced  
17 while the magnitude of the photocurrent recombination transients increased and the oxidation  
18 onset potential was shifted by  $\sim 90$  mV to a more oxidative potential (Figure S21), suggesting  
19 that increasing the concentration of  $\text{Cu}^{2+}$  increased the number of charge-carrier  
20 recombination sites and hindered the catalytic activity observed, in agreement with existing  
21 reports regarding Cu-doped  $\text{TiO}_2$  for the photocatalytic oxidation of methylene blue.<sup>62</sup>  
22 Furthermore, it has been reported that the optimal Cu dopant concentration is  $\sim 0.5$  at.%,<sup>88</sup>  
23 thus increasing the Cu concentration did not improve the PEC activity.  
24  
25  
26  
27  
28  
29  
30  
31  
32  
33  
34  
35  
36  
37  
38  
39  
40  
41  
42  
43  
44  
45  
46  
47  
48  
49  
50  
51  
52  
53  
54  
55  
56  
57  
58  
59  
60

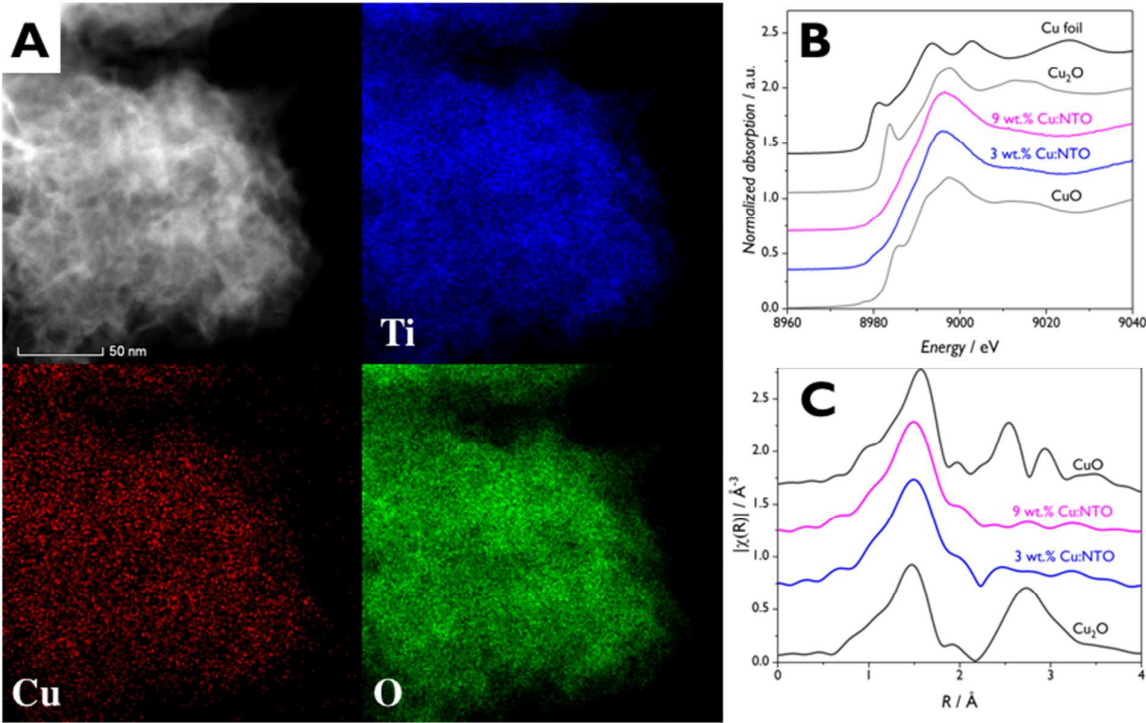


**Figure 6.** (A) HAADF-STEM and corresponding EDS elemental mapping of 9 wt.% Cu:NTO NWs synthesized by cathodic corrosion of Cu<sub>19.32</sub>Ti<sub>80.68</sub> in 10 M NaOH. Comparative (B) normalized XANES and (C) EXAFS Fourier Transforms of  $k^2\chi(k)$  functions for Cu:NTO NWs at the Cu K-edge; metallic foils and standard metal oxide compounds are represented by black lines and grey lines, respectively.

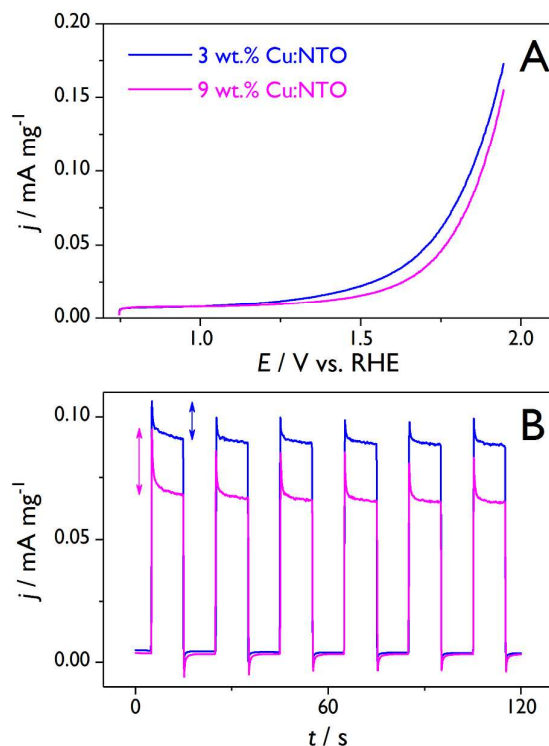


**Figure 7.** (A) Anodic voltammetric profiles of Cu:NTO NWs under incident white polychromatic light normalized by the mass loading of each photocatalyst;  $v=20$  mV s<sup>-1</sup>. (B) Chopped light  $I$ - $t$  curves at 1.8 V vs RHE; arrows correspond to the relative magnitude of recombination-transient photocurrent density for each material.

## Conclusions

We successfully demonstrated the synthesis of mixed metal oxides via the cathodic corrosion of laser-fabricated alloy samples, providing a rapid, electrochemical route for the production, screening and discovery of high surface area nanomaterials with controlled composition. Specifically, we synthesized NTO and M:NTO nanomaterials, where M (= Fe, Cu or Sn) was incorporated into nanowires that agglomerated to generate higher surface area particles.

We explored the synergy between cathodic corrosion and SDA to produce nanostructured mixed metal oxide materials in a single step without the addition of dopant-metal precursors in the electrolyte. The retention of the relative composition of the alloys was best achieved in

the FeTi system, which was essentially identical to the parent alloy. Compositional retention was poorest in the case of SnTi, with noticeable difference between the parent alloy and 25 wt.% Sn:NTO, in addition to a significantly large value of standard deviation, due to the high dopant concentration and multiple crystalline phases of the alloy detected by XRD (Figure S2). A smaller value of standard deviation was observed for 3 wt.% Cu:NTO at the expense of poor retention of composition. Nevertheless, we were able to identify the source of this discrepancy, ascribed to the tendency of Cu ions to form soluble aqueous complexes in the presence of  $\text{OH}^-$  and a maximum concentration of Cu intercalation in the oxide matrix. Good retention of starting relative composition is achieved when optimal cathodic corrosion conditions are employed, which requires consideration of the etching electrolyte is important to this effect.

XRD and HAADF EDS mapping demonstrated that the distribution of elements in the NWs synthesized by cathodic corrosion was homogenous for all samples, while HRTEM imaging demonstrated that the synthesized NWs were crystalline.  $\text{SnO}_2$  rutile phase was observed in the XRD pattern of 25 wt.% Sn:NTO and was attributed to the varying etching rates of different SnTi phases but could be the result of different rates of chemical oxidation upon interaction with dissolved oxygen species. The wide range of relative metal compositions obtained by EDS was due to the presence of  $\text{SnO}_2$  and Sn:NTO phases.

While all samples displayed PEC activity towards oxygen evolution under white light illumination, only 3 wt.% Cu:NTO NWs, displayed a higher activity than undoped NTO. To the best of our knowledge this was the first demonstration of the PEC activity of intercalated copper titanate nanomaterials towards the OER. Exploiting the newly developed ability to modify the atomic percentage of Cu, we explored the effect of increasing it. However, increases in Cu concentration were detrimental to the OER activity. No improvement in PEC activity was observed for 5 wt.% Fe:NTO relative to the undoped NWs. This was attributed

to the Fe(III) oxidation state in the nanostructures which serve as recombination centers for photogenerated charge carrier species.

In summary, this work showcases the ability of the cathodic corrosion method to rapidly produce metal-doped metal oxide nanostructures by the single-step electrochemical etching of alloys at ambient temperature. Future directions in our laboratories will explore the fine control over the size and structure of the nanoparticles, as well as the application of the methodology to a wider range of metal oxide systems and the inclusion of a variety of elements, with higher refinement of dopant concentration, for systematic studies on the impact of compositionally-controlled dopants on the electrochemical performance of metal oxide NWs for applications in energy technologies.

## ASSOCIATED CONTENT

**Supporting Information.** Contains additional experimental details regarding the characterization of the laser fabricated alloys via XRD, XRF and EDX. Additional XRD, SEM-EDX and STEM characterization of the M:NTO NWs. Metal oxidation states as determined by XANES. EXAFS experimental data, FTs and fitting parameters. Additional electrochemical measurements: voltammetry and chronoamperometry.

## AUTHOR INFORMATION

### Corresponding Authors

\* [gum@sustc.edu.cn](mailto:gum@sustc.edu.cn) (Meng Gu); [joaquinr@illinois.edu](mailto:joaquinr@illinois.edu) (Joaquín Rodríguez-López),  
[p.b.rodriguez@bham.ac.uk](mailto:p.b.rodriguez@bham.ac.uk) (Paramaconi Rodriguez)

### Author Contributions

P.R., J.R.-L and M.J.L conceived the experiments. Preparation, XRD, XRF and SEM-EDX characterization of the nanoparticles, electrochemical and photoelectrochemical experiments were performed by M.J.L. XANES and EXAFS characterization and analyses were performed by V.C and P.R. The HRTEM, STEM and HAADF-EDS experiments and analyses were performed by S.X., W.Q and M.J.L. A.Y. contributed to the development and maintenance of the cathodic corrosion system. N.J.E.A. prepared the laser-fabricated alloys. All authors contributed to the analysis of the results, discussion, writing and revision of the manuscript. All authors have given approval to the final version of the manuscript.

## ACKNOWLEDGMENTS

M.J.L acknowledges the University of Birmingham for financial support through Ph.D. scholarships at the School of Chemistry. V.C. and P.R. are thankful to the UK Catalysis Hub (EPSRC grants EP/K014706/1 and EP/K014714/1) for resources and support. The authors wish to acknowledge the Diamond Light Source for provision of beamtime (SP15151). X.S, Q.W. and M.G. wish to acknowledge the SUSTech Pico Center that receives funding from the Shenzhen government, where the STEM analyses were conducted. M.J.L, P.R. and J.R.L acknowledge financial support from the BRIDGE program between the University of Illinois and the University of Birmingham through the Transatlantic Collaboration Fund. P.R. acknowledges the University of Birmingham for financial support through the Birmingham fellowship program.

## REFERENCES

- (1) Neef, H. J. International overview of hydrogen and fuel cell research. *Energy* **2009**, *34*, 327-333, DOI: 10.1016/j.energy.2008.08.014.
- (2) Amirante, R.; Cassone, E.; Distaso, E.; Tamburrano, P. Overview on recent developments in energy storage: Mechanical, electrochemical and hydrogen technologies. *Energy Convers. Manage.* **2017**, *132*, 372-387, DOI: 10.1016/j.enconman.2016.11.046.
- (3) Liang, K.; Li, L.; Yang, Y. Inorganic Porous Films for Renewable Energy Storage. *ACS Energy Lett.* **2017**, *2*, 373-390, DOI: 10.1021/acseenergylett.6b00666.
- (4) Stolarczyk, J. K.; Bhattacharyya, S.; Polavarapu, L.; Feldmann, J. Challenges and Prospects in Solar Water Splitting and CO<sub>2</sub> Reduction with Inorganic and Hybrid Nanostructures. *ACS Catal.* **2018**, *8*, 3602-3635, DOI: 10.1021/acscatal.8b00791.
- (5) Lee, K.; Mazare, A.; Schmuki, P. One-dimensional titanium dioxide nanomaterials: nanotubes. *Chem. Rev.* **2014**, *114*, 9385-454, DOI: 10.1021/cr500061m.
- (6) Zhang, J.; Xiao, G.; Xiao, F.-X.; Liu, B. Revisiting one-dimensional TiO<sub>2</sub> based hybrid heterostructures for heterogeneous photocatalysis: a critical review. *Mater. Chem. Front.* **2017**, *1*, 231-250, DOI: 10.1039/c6qm00141f.
- (7) Ge, M.; Cao, C.; Huang, J.; Li, S.; Chen, Z.; Zhang, K.-Q.; Al-Deyab, S. S.; Lai, Y. A review of one-dimensional TiO<sub>2</sub> nanostructured materials for environmental and energy applications. *J. Mater. Chem. A* **2016**, *4*, 6772-6801, DOI: 10.1039/c5ta09323f.
- (8) Ota, M.; Hirota, Y.; Uchida, Y.; Sakamoto, Y.; Nishiyama, N. Low Temperature Synthesized H<sub>2</sub>Ti<sub>3</sub>O<sub>7</sub> Nanotubes with a High CO<sub>2</sub> Adsorption Property by Amine Modification. *Langmuir* **2018**, *34*, 6814-6819, DOI: 10.1021/acs.langmuir.8b00317.



(9) Liu, J.; Banis, M. N.; Xiao, B.; Sun, Q.; Lushington, A.; Li, R.; Guo, J.; Sham, T.-K.; Sun, X. Atomically precise growth of sodium titanates as anode materials for high-rate and ultralong cycle-life sodium-ion batteries. *J. Mater. Chem. A* **2015**, *3*, 24281-24288, DOI: 10.1039/c5ta08435k.

(10) Chen, Z.; Belharouak, I.; Sun, Y. K.; Amine, K. Titanium-Based Anode Materials for Safe Lithium-Ion Batteries. *Adv. Funct. Mater.* **2013**, *23*, 959-969, DOI: 10.1002/adfm.201200698.

(11) Li, C.; Wang, Z.; Li, S.; Cheng, J.; Zhang, Y.; Zhou, J.; Yang, D.; Tong, D.-G.; Wang, B. Interfacial Engineered Polyaniline/Sulfur-Doped TiO<sub>2</sub> Nanotube Arrays for Ultralong Cycle Lifetime Fiber-Shaped, Solid-State Supercapacitors. *ACS Appl. Mater. Interfaces* **2018**, *10*, 18390-18399, DOI: 10.1021/acsami.8b01160.

(12) Lu, X.; Wang, G.; Zhai, T.; Yu, M.; Gan, J.; Tong, Y.; Li, Y. Hydrogenated TiO<sub>2</sub> nanotube arrays for supercapacitors. *Nano Lett* **2012**, *12*, 1690-6, DOI: 10.1021/nl300173j.

(13) Zhou, W.; Liu, X.; Sang, Y.; Zhao, Z.; Zhou, K.; Liu, H.; Chen, S. Enhanced performance of layered titanate nanowire-based supercapacitor electrodes by nickel ion exchange. *ACS Appl Mater Interfaces* **2014**, *6*, 4578-86, DOI: 10.1021/am500421r.

(14) Chu, L.; Qin, Z.; Yang, J.; Li, X. a. Anatase TiO<sub>2</sub> Nanoparticles with Exposed {001} Facets for Efficient Dye-Sensitized Solar Cells. *Sci. Rep.* **2015**, *5*, DOI: 10.1038/srep12143.

(15) Sarkar, K.; Braden, E. V.; Fröschl, T.; Hüsing, N.; Müller-Buschbaum, P. Spray-deposited zinc titanate films obtained via sol-gel synthesis for application in dye-sensitized solar cells. *J. Mater. Chem. A* **2014**, *2*, 15008-15014, DOI: 10.1039/c4ta02031f.

(16) Li, K.; Xu, J.; Shi, W.; Wang, Y.; Peng, T. Synthesis of size controllable and thermally stable rice-like brookite titania and its application as a scattering layer for nano-sized titania

1  
2  
3 film-based dye-sensitized solar cells. *J. Mater. Chem. A* **2014**, *2*, 1886-1896, DOI:  
4 10.1039/c3ta13597g.  
5  
6

7  
8 (17) Ma, Y.; Wang, X.; Jia, Y.; Chen, X.; Han, H.; Li, C. Titanium Dioxide-Based  
9 Nanomaterials for Photocatalytic Fuel Generations. *Chem. Rev.* **2014**, *114*, 9987-10043, DOI:  
10 10.1021/cr500008u.  
11  
12

13  
14  
15 (18) Reyes-Gil, K. R.; Robinson, D. B. WO<sub>3</sub>-enhanced TiO<sub>2</sub> nanotube photoanodes for  
16 solar water splitting with simultaneous wastewater treatment. *ACS Appl. Mater. Interfaces*  
17 **2013**, *5*, 12400-10, DOI: 10.1021/am403369p.  
18  
19

20  
21  
22 (19) Simpson, B. H.; Rodríguez-López, J. Emerging techniques for the in situ analysis of  
23 reaction intermediates on photo-electrochemical interfaces. *Analytical Methods* **2015**, *7*,  
24 7029-7041, DOI: 10.1039/c5ay00503e.  
25  
26

27  
28  
29 (20) Chen, X.; Shen, S.; Guo, L.; Mao, S. S. Semiconductor-based photocatalytic hydrogen  
30 generation. *Chem. Rev.* **2010**, *110*, 6503-70, DOI: 10.1021/cr1001645.  
31  
32

33  
34  
35 (21) Cai, J.; Wu, X.; Li, S.; Zheng, F. Synthesis of TiO<sub>2</sub>@WO<sub>3</sub>/Au Nanocomposite  
36 Hollow Spheres with Controllable Size and High Visible-Light-Driven Photocatalytic  
37 Activity. *ACS Sustainable Chem. Eng.* **2016**, *4*, 1581-1590, DOI:  
38 10.1021/acssuschemeng.5b01511.  
39  
40  
41

42  
43  
44 (22) Zhang, X.; Liu, Y.; Lee, S.-T.; Yang, S.; Kang, Z. Coupling surface plasmon  
45 resonance of gold nanoparticles with slow-photon-effect of TiO<sub>2</sub> photonic crystals for  
46 synergistically enhanced photoelectrochemical water splitting. *Energy Environ. Sci.* **2014**, *7*,  
47 DOI: 10.1039/c3ee43278e.  
48  
49  
50

51  
52  
53 (23) Graetzel, M.; Howe, R. F. Electron paramagnetic resonance studies of doped titanium  
54 dioxide colloids. *J. Phys. Chem.* **1990**, *94*, 2566-2572, DOI: 10.1021/j100369a064.  
55  
56  
57

(24) Choi, W.; Termin, A.; Hoffmann, M. R. Effects of Metal-Ion Dopants on the Photocatalytic Reactivity of Quantum-Sized TiO<sub>2</sub> Particles. *Angew. Chem., Int. Ed.* **1994**, *33*, 1091-1092, DOI: 10.1002/anie.199410911.

(25) Khan, M.; Woo, S.; Yang, O. Hydrothermally stabilized Fe(III) doped titania active under visible light for water splitting reaction. *Int. J. Hydrogen Energy* **2008**, *33*, 5345-5351, DOI: 10.1016/j.ijhydene.2008.07.119.

(26) Ganesh, I.; Kumar, P. P.; Annapoorna, I.; Sumliner, J. M.; Ramakrishna, M.; Hebalkar, N. Y.; Padmanabham, G.; Sundararajan, G. Preparation and characterization of Cu-doped TiO<sub>2</sub> materials for electrochemical, photoelectrochemical, and photocatalytic applications. *Appl. Surf. Sci.* **2014**, *293*, 229-247, DOI: 10.1016/j.apsusc.2013.12.140.

(27) Liu, Y.; Liang, W.; Zhang, W.; Zhang, J.; Han, P. First principle study of Cu-N, Cu and N-doped anatase TiO<sub>2</sub>. *Solid State Commun.* **2013**, *164*, 27-31, DOI: 10.1016/j.ssc.2013.04.005.

(28) Ako, R. T.; Ekanayake, P.; Young, D. J.; Hobley, J.; Chellappan, V.; Tan, A. L.; Gorelik, S.; Subramanian, G. S.; Lim, C. M. Evaluation of surface energy state distribution and bulk defect concentration in DSSC photoanodes based on Sn, Fe, and Cu doped TiO<sub>2</sub>. *Appl. Surf. Sci.* **2015**, *351*, 950-961, DOI: 10.1016/j.apsusc.2015.06.015.

(29) Moradi, H.; Eshaghi, A.; Hosseini, S. R.; Ghani, K. Fabrication of Fe-doped TiO<sub>2</sub> nanoparticles and investigation of photocatalytic decolorization of reactive red 198 under visible light irradiation. *Ultrason. Sonochem.* **2016**, *32*, 314-319, DOI: 10.1016/j.ultsonch.2016.03.025.

(30) Duan, Y.; Fu, N.; Liu, Q.; Fang, Y.; Zhou, X.; Zhang, J.; Lin, Y. Sn-Doped TiO<sub>2</sub> Photoanode for Dye-Sensitized Solar Cells. *J. Phys. Chem. C* **2012**, *116*, 8888-8893, DOI: 10.1021/jp212517k.

(31) Morgado, E.; Marinkovic, B. A.; Jardim, P. M.; de Abreu, M. A. S.; Rocha, M. d. G. C.; Bargiela, P. Studies on Fe-modified nanostructured trititanates. *Mater. Chem. Phys.* **2011**, *126*, 118-127, DOI: 10.1016/j.matchemphys.2010.11.054.

(32) Peter, L. M.; Upul Wijayantha, K. G. Photoelectrochemical water splitting at semiconductor electrodes: fundamental problems and new perspectives. *ChemPhysChem* **2014**, *15*, 1983-95, DOI: 10.1002/cphc.201402024.

(33) Morgan, D. L.; Triani, G.; Blackford, M. G.; Raftery, N. A.; Frost, R. L.; Waclawik, E. R. Alkaline hydrothermal kinetics in titanate nanostructure formation. *J. Mater. Sci.* **2011**, *46*, 548-557, DOI: 10.1007/s10853-010-5016-0.

(34) Xia, J.; Zhao, H.; Pang, W. K.; Yin, Z.; Zhou, B.; He, G.; Guo, Z.; Du, Y. Lanthanide doping induced electrochemical enhancement of Na<sub>2</sub>Ti<sub>3</sub>O<sub>7</sub> anodes for sodium-ion batteries. *Chem. Sci.* **2018**, *9*, 3421-3425, DOI: 10.1039/c7sc05185a.

(35) Bavykin, D. V.; Friedrich, J. M.; Walsh, F. C. Protonated Titanates and TiO<sub>2</sub> Nanostructured Materials: Synthesis, Properties, and Applications. *Adv. Mater.* **2006**, *18*, 2807-2824, DOI: 10.1002/adma.200502696.

(36) Aaltonen, T.; Alnes, M.; Nilsen, O.; Costelle, L.; Fjellvåg, H. Lanthanum titanate and lithium lanthanum titanate thin films grown by atomic layer deposition. *J. Mater. Chem.* **2010**, *20*, DOI: 10.1039/b923490j.

(37) Kasuga, T.; Hiramatsu, M.; Hoson, A.; Sekino, T.; Niihara, K. Formation of Titanium Oxide Nanotube. *Langmuir* **1998**, *14*, 3160-3163, DOI: 10.1021/la9713816.

(38) An, Y.; Li, Z.; Shen, J. The visible light absorption property of Cu-doped hydrogen titanate nanotube thin films: An experimental and theoretical study. *Phys. B (Amsterdam, Neth.)* **2013**, *429*, 127-132, DOI: 10.1016/j.physb.2013.08.006.

(39) dos Santos, N. M.; Rocha, J. M.; Matos, J. M. E.; Ferreira, O. P.; Filho, J. M.; Viana, B. C.; Oliveira, A. C. Metal cations intercalated titanate nanotubes as catalysts for  $\alpha,\beta$  unsaturated esters production. *Appl. Catal., A* **2013**, *454*, 74-80, DOI: 10.1016/j.apcata.2012.12.035.

(40) Wen, W.; Wu, J.-m.; Jiang, Y.-z.; Yu, S.-l.; Bai, J.-q.; Cao, M.-h.; Cui, J. Anatase TiO<sub>2</sub> ultrathin nanobelts derived from room-temperature-synthesized titanates for fast and safe lithium storage. *Sci. Rep.* **2015**, *5*, 959-969, DOI: 10.1038/srep11804.

(41) Kromer, M. L.; Monzo, J.; Lawrence, M. J.; Kolodziej, A.; Gossage, Z. T.; Simpson, B. H.; Morandi, S.; Yanson, A.; Rodriguez-Lopez, J.; Rodriguez, P. High-Throughput Preparation of Metal Oxide Nanocrystals by Cathodic Corrosion and Their Use as Active Photocatalysts. *Langmuir* **2017**, *33*, 13295-13302, DOI: 10.1021/acs.langmuir.7b02465.

(42) Lawrence, M. J.; Kolodziej, A.; Rodriguez, P. Controllable synthesis of nanostructured metal oxide and oxyhydroxide materials via electrochemical methods. *Curr. Opin. Electrochem.* **2018**, *Article in Press*, DOI: 10.1016/j.coelec.2018.03.014.

(43) Endrődi, B.; Kecsenvity, E.; Rajeshwar, K.; Janáky, C. One-Step Electrodeposition of Nanocrystalline TiO<sub>2</sub> Films with Enhanced Photoelectrochemical Performance and Charge Storage. *ACS Appl. Energy Mater.* **2018**, *1*, 851-858, DOI: 10.1021/acsaem.7b00289.

(44) Su, T.-S.; Wu, Y.-S.; Tung, Y.-L.; Wei, T.-C. One-Pot Electrodeposition of Compact Layer and Mesoporous Scaffold for Perovskite Solar Cells. *ACS Appl. Energy Mater.* **2018**, *1*, 2429-2433, DOI: 10.1021/acsaem.8b00566.

(45) Nguyen, N. T.; Hwang, I.; Kondo, T.; Yanagishita, T.; Masuda, H.; Schmuki, P. Optimizing TiO<sub>2</sub> nanotube morphology for enhanced photocatalytic H<sub>2</sub> evolution using single-walled and highly ordered TiO<sub>2</sub> nanotubes decorated with dewetted Au nanoparticles. *Electrochem. Commun.* **2017**, *79*, 46-50, DOI: 10.1016/j.elecom.2017.04.016.

(46) Qiu, C.; Ravi, G. A.; Dance, C.; Ranson, A.; Dilworth, S.; Attallah, M. M. Fabrication of large Ti–6Al–4V structures by direct laser deposition. *J. Alloys Compd.* **2015**, *629*, 351-361, DOI: 10.1016/j.jallcom.2014.12.234.

(47) Garcia-Canadas, J.; Adkins, N. J.; McCain, S.; Hauptstein, B.; Brew, A.; Jarvis, D. J.; Min, G. Accelerated Discovery of Thermoelectric Materials: Combinatorial Facility and High-Throughput Measurement of Thermoelectric Power Factor. *ACS Comb. Sci.* **2016**, *18*, 314-319, DOI: 10.1021/acscombsci.5b00178.

(48) Yanson, A. I.; Rodriguez, P.; Garcia-Araez, N.; Mom, R. V.; Tichelaar, F. D.; Koper, M. T. Cathodic corrosion: a quick, clean, and versatile method for the synthesis of metallic nanoparticles. *Angew. Chem., Int. Ed.* **2011**, *50*, 6346-50, DOI: 10.1002/anie.201100471.

(49) Rodriguez, P.; Tichelaar, F. D.; Koper, M. T.; Yanson, A. I. Cathodic corrosion as a facile and effective method to prepare clean metal alloy nanoparticles. *J. Am. Chem. Soc.* **2011**, *133*, 17626-9, DOI: 10.1021/ja208264e.

(50) Vanrenterghem, B.; Bele, M.; Zepeda, F. R.; Šala, M.; Hodnik, N.; Breugelmans, T. Cutting the Gordian Knot of electrodeposition via controlled cathodic corrosion enabling the production of supported metal nanoparticles below 5 nm. *Appl. Catal., B* **2018**, *226*, 396-402, DOI: 10.1016/j.apcatb.2017.12.080.

(51) Yanson, A. I.; Antonov, P. V.; Rodriguez, P.; Koper, M. T. M. Influence of the electrolyte concentration on the size and shape of platinum nanoparticles synthesized by

cathodic corrosion. *Electrochim. Acta* **2013**, *112*, 913-918, DOI: 10.1016/j.electacta.2013.01.056.

(52) Bennett, E.; Monzó, J.; Humphrey, J.; Plana, D.; Walker, M.; McConville, C.; Fermin, D.; Yanson, A.; Rodriguez, P. A Synthetic Route for the Effective Preparation of Metal Alloy Nanoparticles and Their Use as Active Electrocatalysts. *ACS Catal.* **2016**, *6*, 1533-1539, DOI: 10.1021/acscatal.5b02598.

(53) Simonet, J. The platinized platinum interface in super-dry solvents: Cathodic reversible reactivity and morphology modifications in the presence of tetramethylammonium salts. *Journal of Electroanalytical Chemistry* **2006**, *593*, 3-14, DOI: 10.1016/j.jelechem.2006.01.019.

(54) Ghilane, J.; Guilloux-Viry, M.; Lagrost, C.; Simonet, J.; Hapiot, P. Reactivity of platinum metal with organic radical anions from metal to negative oxidation states. *J Am Chem Soc* **2007**, *129*, 6654-61, DOI: 10.1021/ja071483a.

(55) Lu, F.; Ji, X.; Yang, Y.; Deng, W.; Banks, C. E. Room temperature ionic liquid assisted well-dispersed core-shell tin nanoparticles through cathodic corrosion. *RSC Adv.* **2013**, *3*, DOI: 10.1039/c3ra43532f.

(56) Dent, A. J.; Cibir, G.; Ramos, S.; Smith, A. D.; Scott, S. M.; Varandas, L.; Pearson, M. R.; Krumpa, N. A.; Jones, C. P.; Robbins, P. E. B18: A core XAS spectroscopy beamline for Diamond. *J. Phys.: Conf. Ser.* **2009**, *190*, DOI: 10.1088/1742-6596/190/1/012039.

(57) Newville, M. EXAFS analysis using FEFF and FEFFIT. *J. Synchrotron Radiat.* **2001**, *8*, 96-100, DOI: 10.1107/s0909049500016290.

(58) Ravel, B.; Newville, M. ATHENA, ARTEMIS, HEPHAESTUS: data analysis for X-ray absorption spectroscopy using IFEFFIT. *J. Synchrotron Radiat.* **2005**, *12*, 537-41, DOI: 10.1107/S0909049505012719.

(59) Du, G. H.; Chen, Q.; Che, R. C.; Yuan, Z. Y.; Peng, L. M. Preparation and structure analysis of titanium oxide nanotubes. *Appl. Phys. Lett.* **2001**, *79*, 3702-3704, DOI: 10.1063/1.1423403.

(60) Umek, P.; Pregelj, M.; Gloter, A.; Cevc, P.; Jagličić, Z.; Čeh, M.; Pirnat, U.; Arčon, D. Coordination of Intercalated Cu<sup>2+</sup> Sites in Copper Doped Sodium Titanate Nanotubes and Nanoribbons. *J. Phys. Chem. C* **2008**, *112*, 15311-15319, DOI: 10.1021/jp805005k.

(61) Rudola, A.; Saravanan, K.; Mason, C. W.; Balaya, P. Na<sub>2</sub>Ti<sub>3</sub>O<sub>7</sub>: an intercalation based anode for sodium-ion battery applications. *J. Mater. Chem. A* **2013**, *1*, DOI: 10.1039/c2ta01057g.

(62) Bensouici, F.; Bououdina, M.; Dakhel, A. A.; Tala-Ighil, R.; Tounane, M.; Iratni, A.; Souier, T.; Liu, S.; Cai, W. Optical, structural and photocatalysis properties of Cu-doped TiO<sub>2</sub> thin films. *Appl. Surf. Sci.* **2017**, *395*, 110-116, DOI: 10.1016/j.apsusc.2016.07.034.

(63) Yamanaka, T.; Kurashima, R.; Mimaki, J. X-ray diffraction study of bond character of rutile-type SiO<sub>2</sub>, GeO<sub>2</sub> and SnO<sub>2</sub>. *Z. Kristallogr.* **2000**, *215*, DOI: 10.1524/zkri.2000.215.7.424.

(64) Akila, Y.; Muthukumarasamy, N.; Agilan, S.; Senthilarasu, S.; Velauthapillai, D. Zirconium oxide post treated tin doped TiO<sub>2</sub> for dye sensitized solar cells. *Mater. Sci. Semicond. Process.* **2017**, *57*, 24-31, DOI: 10.1016/j.mssp.2016.09.028.



(65) Rodriguez, P.; Plana, D.; Fermin, D. J.; Koper, M. T. M. New insights into the catalytic activity of gold nanoparticles for CO oxidation in electrochemical media. *J. Catal.* **2014**, *311*, 182-189, DOI: 10.1016/j.jcat.2013.11.020.

(66) Feng, J.; Chen, D.; Sediq, A. S.; Romeijn, S.; Tichelaar, F. D.; Jiskoot, W.; Yang, J.; Koper, M. T. M. Cathodic Corrosion of a Bulk Wire to Nonaggregated Functional Nanocrystals and Nanoalloys. *ACS Appl. Mater. Interfaces* **2018**, *10*, 9532-9540, DOI: 10.1021/acsami.7b18105.

(67) Kuhn, J. N.; Tsung, C.-K.; Huang, W.; Somorjai, G. A. Effect of organic capping layers over monodisperse platinum nanoparticles upon activity for ethylene hydrogenation and carbon monoxide oxidation. *J. Catal.* **2009**, *265*, 209-215, DOI: 10.1016/j.jcat.2009.05.001.

(68) Vidal-Iglesias, F. J.; Solla-Gullón, J.; Herrero, E.; Montiel, V.; Aldaz, A.; Feliu, J. M. Evaluating the ozone cleaning treatment in shape-controlled Pt nanoparticles: Evidences of atomic surface disordering. *Electrochem. Commun.* **2011**, *13*, 502-505, DOI: 10.1016/j.elecom.2011.02.033.

(69) Monzo, J.; Koper, M. T.; Rodriguez, P. Removing polyvinylpyrrolidone from catalytic Pt nanoparticles without modification of superficial order. *ChemPhysChem* **2012**, *13*, 709-15, DOI: 10.1002/cphc.201100894.

(70) Ding, X.; Xu, X. G.; Chen, Q.; Peng, L. M. Preparation and characterization of Fe-incorporated titanate nanotubes. *Nanotechnology* **2006**, *17*, 5423-5427, DOI: 10.1088/0957-4484/17/21/023.

(71) Huang, C.; Liu, X.; Kong, L.; Lan, W.; Su, Q.; Wang, Y. The structural and magnetic properties of Co-doped titanate nanotubes synthesized under hydrothermal conditions. *Appl. Phys. A* **2007**, *87*, 781-786, DOI: 10.1007/s00339-007-3902-3.

(72) Kasian, P.; Yamwong, T.; Thongbai, P.; Rujirawat, S.; Yimnirun, R.; Maensiri, S. Co-doped titanate nanotubes: Synthesis, characterization, and properties. *Jpn. J. Appl. Phys.* **2014**, *53*, DOI: 10.7567/jjap.53.06jg12.

(73) Wu, D.; Chen, Y.; Liu, J.; Zhao, X.; Li, A.; Ming, N. Co-doped titanate nanotubes. *Appl. Phys. Lett.* **2005**, *87*, DOI: 10.1063/1.2043254.

(74) Umek, P.; Bittencourt, C.; Gloter, A.; Dominko, R.; Jagličić, Z.; Cevc, P.; Arčon, D. Local Coordination and Valence States of Cobalt in Sodium Titanate Nanoribbons. *J. Phys. Chem. C* **2012**, *116*, 11357-11363, DOI: 10.1021/jp3012238.

(75) Waychunas, G. A. Synchrotron Radiation Xanes Spectroscopy of Ti in Minerals - Effects of Ti Bonding Distances, Ti Valence, and Site Geometry on Absorption-Edge Structure. *Am. Mineral.* **1987**, *72*, 89-101.

(76) Farges, F.; Brown, G. E.; Rehr, J. J. Ti K-edge XANES studies of Ti coordination and disorder in oxide compounds: Comparison between theory and experiment. *Phys. B (Amsterdam, Neth.)* **1997**, *56*, 1809-1819, DOI: 10.1103/PhysRevB.56.1809.

(77) Piquer, C.; Laguna-Marco, M. A.; Roca, A. G.; Boada, R.; Guglieri, C.; Chaboy, J. Fe K-Edge X-ray Absorption Spectroscopy Study of Nanosized Nominal Magnetite. *J. Phys. Chem. C* **2014**, *118*, 1332-1346, DOI: 10.1021/jp4104992.

(78) Liu, F.; Asakura, K.; Xie, P.; Wang, J.; He, H. An XAFS study on the specific microstructure of active species in iron titanate catalyst for NH<sub>3</sub>-SCR of NO<sub>x</sub>. *Catal. Today* **2013**, *201*, 131-138, DOI: 10.1016/j.cattod.2012.03.062.

(79) Gaur, A.; Shrivastava, B. D. A Comparative Study of the Methods of Speciation Using X-ray Absorption Fine Structure. *Acta Phys. Pol., A* **2012**, *121*, 647-652, DOI: 10.12693/APhysPolA.121.647.

(80) Chen, C. S.; Chen, C. C.; Lai, T. W.; Wu, J. H.; Chen, C. H.; Lee, J. F. Water Adsorption and Dissociation on Cu Nanoparticles. *J. Phys. Chem. C* **2011**, *115*, 12891-12900, DOI: 10.1021/jp200478r.

(81) Chen, C. S.; Chen, T. C.; Chen, C. C.; Lai, Y. T.; You, J. H.; Chou, T. M.; Chen, C. H.; Lee, J. F. Effect of Ti<sup>3+</sup> on TiO<sub>2</sub>-supported Cu catalysts used for CO oxidation. *Langmuir* **2012**, *28*, 9996-10006, DOI: 10.1021/la301684h.

(82) Dalpian, G. M.; Liu, Q.; Stoumpos, C. C.; Douvalis, A. P.; Balasubramanian, M.; Kanatzidis, M. G.; Zunger, A. Changes in charge density vs changes in formal oxidation states: The case of Sn halide perovskites and their ordered vacancy analogues. *Phys. Rev. Mater.* **2017**, *1*, DOI: 10.1103/PhysRevMaterials.1.025401.

(83) Khemthong, P.; Photai, P.; Grisdanurak, N. Structural properties of CuO/TiO<sub>2</sub> nanorod in relation to their catalytic activity for simultaneous hydrogen production under solar light. *Int. J. Hydrogen Energy* **2013**, *38*, 15992-16001, DOI: 10.1016/j.ijhydene.2013.10.065.

(84) Sharma, A.; Varshney, M.; Park, J.; Ha, T.-K.; Chae, K.-H.; Shin, H.-J. XANES, EXAFS and photocatalytic investigations on copper oxide nanoparticles and nanocomposites. *RSC Adv.* **2015**, *5*, 21762-21771, DOI: 10.1039/c4ra16217j.

(85) Kavan, L.; Grätzel, M. Highly efficient semiconducting TiO<sub>2</sub> photoelectrodes prepared by aerosol pyrolysis. *Electrochim. Acta* **1995**, *40*, 643-652, DOI: 10.1016/0013-4686(95)90400-w.

(86) Wang, Y.; Cheng, H.; Hao, Y.; Ma, J.; Li, W.; Cai, S. Preparation, characterization and photoelectrochemical behaviours of Fe(III)-doped TiO<sub>2</sub> nanoparticles. *J. Mater. Sci.* **1999**, *34*, 3721-3729, DOI: 10.1023/a:1004611724069.

(87) Zhou, L.; Wei, L.; Yang, Y.; Xia, X.; Wang, P.; Yu, J.; Luan, T. Improved performance of dye sensitized solar cells using Cu-doped TiO<sub>2</sub> as photoanode materials: Band edge movement study by spectroelectrochemistry. *Chemical Physics* **2016**, *475*, 1-8, DOI: 10.1016/j.chemphys.2016.05.018.

(88) Colón, G.; Maicu, M.; Hidalgo, M. C.; Navío, J. A. Cu-doped TiO<sub>2</sub> systems with improved photocatalytic activity. *Appl. Catal., B* **2006**, *67*, 41-51, DOI: 10.1016/j.apcatb.2006.03.019.

TOC GRAPHICS

